Nano Research

Open Access

Research Article

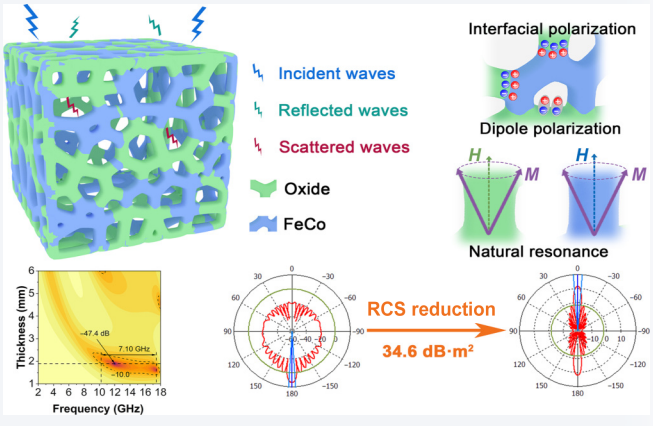
Confinement engineering of FeCo magnetoelectric composite nanocages for enhanced magnetic loss and wideband electromagnetic wave absorption

Huipeng Lv[1,2], Panbin Zhu[1], Ji Teng[1], Mi Yan[1], Guang Liu[1]✉, and Chen Wu[1]✉

[1] School of Materials Science and Engineering, State Key Laboratory of Silicon and Advanced Semiconductor Materials, Zhejiang University, Hangzhou 310058, China
[2] Ordered Matter Science Research Center, Nanchang University, Nanchang 330031, China

Cite this article: *Nano Research*, **2026**, *19*, 94908356. https://doi.org/10.26599/NR.2026.94908356

ABSTRACT: Electromagnetic (EM) wave absorbers with strong attenuation over a broad frequency range are critical for radiation protection and military stealth. However, magnetic alloys with high dissipation capacity remain challenging to achieve satisfactory impedance matching and enhanced high-frequency magnetic loss due to the scarcity of rational design for the distribution and size of magnetic particles. Herein, we design Prussian blue analogue (PBA) derived FeCo magnetoelectric composite nanocages by confinement engineering, achieving a strong absorption capacity of −47.4 dB and a broad bandwidth of 7.10 GHz at a small thickness of 1.9 mm. The exceptional absorption performance arises, on one hand, from the formation of well-dispersed FeCo nanoparticles with quasi-single-domain size, giving rise to enhanced magnetic anisotropy and high-frequency magnetic resonance. On the other hand, the formation of ferrimagnetic $CoFe_2O_4$ space-confined phase mitigates magnetic dilution, while effectively improving dielectric polarization and impedance matching due to their semiconducting feature. This work not only sheds light on the fabrication of FeCo magnetoelectric composite nanocages as efficient and wideband EM wave absorbers, but also propose a confinement engineering strategy for rational design of functional nanocomposites in multiple fields such as electromagnetics, electronics and optoelectronics.



KEYWORDS: Prussian-blue analogue, magnetoelectric composite nanocages, confinement effect, natural resonance, electromagnetic wave absorption

1 Introduction

The ever-increasing electromagnetic (EM) wave bands employed in electronic devices and detection radars have spawn an urgent demand for advanced EM wave absorbers with wideband dissipation capabilities to mitigate EM interference and radiation [1–7]. A range of material species have been investigated as absorbers, encompassing dielectrics, alloys, polymers, and carbon materials [8–13]. Magnetic materials including soft magnetic alloys and ferrites are regarded as highly promising due to their abundant loss mechanisms involving conductive/dielectric and magnetic attenuation [14–20]. Among them, magnetic alloys such as FeCo stands out as an efficient absorber benefitted from their high saturation magnetization and permeability [21–27]. Nevertheless, the high electrical conductivity of magnetic alloys may lead to poor impedance matching, meanwhile the Snoek's limit inherently restricts their high-frequency permeability and magnetic resonances [28], which ultimately impedes their attenuation capability in the high-frequency band.

Integrating FeCo alloys with insulating or semiconducting materials provides an effective strategy to optimize impedance matching. The isolating effect of low-conductivity materials enables spatial separation of FeCo particles, thereby suppressing severe

Received: November 1, 2025; **Revised:** December 11, 2025
Accepted: December 17, 2025

✉Address correspondence to Guang Liu, guang_liu@zju.edu.cn; Chen Wu, chen_wu@zju.edu.cn

aggregation and excessive conductivity [29, 30]. For instance, Zhong et al. synthesized core–shell structured FeCo@SiO_2@$LiAlSiO_3$ microspheres. Compared to single FeCo particles, the introduction of SiO_2 and silicate effectively improves impedance matching and electromagnetic wave absorption [31]. However, nonmagnetic components in such composite systems often trigger magnetic dilution effects, resulting in reduced permeability and deteriorated magnetic loss. More notably, the *ex-situ* synthesis methods employed in composite preparation hinder precise control over the size and dispersity of FeCo particles, leading to a formidable difficulty in preparing single-domain magnetic particles for strong anisotropy and high-frequency magnetic loss. For example, Gao et al. fabricated ZnO nanoflower decorated FeCo nanoparticles via two-step hydrothermal reaction for enhanced electrical resistivity, while the FeCo/ZnO composites exhibit low magnetic loss and limited bandwidth of 3.80 GHz [32]. Consequently, rational design of FeCo composite absorbers with exceptional impedance matching and strong dissipation ability remains challenging.

In this work, hollow FeCo magnetoelectric composite nanocages have been fabricated via etching and thermal reduction of FeCo-based PBA. The *in-situ* preparation process induces confinement effect between $CoFe_2O_4$ and FeCo phases. Therefore, well-dispersed FeCo nanoparticles with quasi-single-domain size have been obtained, giving rise to enhanced surface anisotropy and natural resonance. The formation of ferrimagnetic $CoFe_2O_4$ space-confined phase mitigates magnetic dilution effects and provides abundant heterointerfaces for improved polarization loss and impedance matching benefitted from intrinsic semiconducting feature. As such the FeCo magnetoelectric composite exhibit excellent EM wave absorption with a minimum reflection loss (RL) of −47.4 dB and broad effective absorption bandwidth (EAB, RL < −10 dB) of 7.10 GHz at a small thickness of 1.9 mm. This work not only demonstrates the superior EM wave absorption performance of FeCo magnetoelectric composite nanocages, but also offers insights for the rational design of magnetic composite materials for diverse EM functional applications.

2 Experimental

2.1 Fabrication of magnetoelectric composite nanocages

FeCo-PBA nanocubes were firstly prepared by co-precipitation method. Typically, $CoCl_2$ (156 mg), sodium citrate (876 mg), and polyvinylpyrrolidone (PVP, K30, 600 mg) were added into 40.0 mL deionized (DI) water under constant stirring. Meanwhile, $K_3[Fe(CN)_6]$ (264 mg) was dissolved into 40.0 mL DI water. The two solutions were then mixed together under vigorous agitation for 10 min, prior to aging at room temperature for 24 h. The precipitates were collected by centrifugation and drying. To fabricate FeCo alloy/oxide nanocages, the obtained FeCo-PBA nanocubes (40 mg) were dispersed into 35.0 mL DI water with the assistance of PVP (K30, 200 mg), followed by ultrasonic bath (100 kHz, 300 W) for 10 min. Then 7.892 g hydrochloric acid (38 wt.%) was added into the solution, followed by constant stirring for 2 h. The viscous solution was then transferred into a stainless autoclave and heated to 120 °C for 2 h, followed by centrifugation and drying. The $CoFe_2O_4$/Co_3O_4 nanocage (denoted as S1) was fabricated by annealing treatment of FeCo-PBA nanocages at 450 °C for 1 h with a heating rate of 2 °C/min under air atmosphere. To obtain FeCo/$CoFe_2O_4$ and FeCo nanocages, the S1 was further annealed at 350 °C for 30, 45, and 60 min under Ar&H_2 atmosphere (10 vol.% H_2) respectively, which are denoted as S2, S3, and S4, respectively.

2.2 Characterization and performance evaluation

Phase structure of the samples was characterized by X-ray diffraction (XRD, D8 Advance, Bruker) with Cu Kα radiation (λ = 0.154 nm). The surface morphology and detailed microstructure were studied via scanning electron microscopy (SEM, S-4800, Hitachi) and transmission electron microscopy (TEM, JEM 2100F, JEOL) equipped with selected area electron diffraction (SAED). Hysteresis loops of the samples were measured by a superconducting quantum interference device (SQUID, MPMS-XL-5, Quantum Design). Chemical composition was measured by an inductively coupled plasma optical emission spectrometer (ICP-OES, iCAP 6300, ThermoFisher). To investigate the EM properties, the sample powders were mixed with paraffin at a mass ratio of 45 wt.% prior to compressing into toroidal cores (φ_{out} = 7.00 mm, φ_{in} = 3.04 mm, height = 2 mm). The relative complex permittivity and permeability were measured via the coaxial method in the frequency range of 2–18 GHz with a vector network analyzer (VNA, PNA-L N5234A, Keysight).

2.3 Simulation

The three-dimensional (3D) radar cross-section (RCS) simulations were conducted using the CST Microwave Studio 2024 to reveal the practical EM absorbing capability in real space. A 180 mm × 180 mm square model positioned in the *X*–O–*Y* plane was constructed with a two-layer configuration: the upper layer corresponds to the absorber with a thickness matching the actual sample, and the lower one comprises a 1.0 mm-thick perfect electrical conductor (PEC). Electromagnetic waves within the linear polarization plane propagate along the negative *Z*-axis, with their electric polarization oriented along the *X*-axis. Fully open boundary conditions were adopted for all simulation processes. Monitoring parameters for electromagnetic waves were determined based on the frequency and thickness corresponding to the minimum reflection loss of each sample. RCS values (σ, dB·m^2) were simulated with reference to [33, 34]

$$\sigma = 10\lg\left(\frac{4\pi S}{\lambda^2}\left|\frac{E_s}{E_i}\right|^2\right) \quad (1)$$

where S is the area of the simulation model, λ stands for the wavelength of the electromagnetic wave, and E_s and E_i refer to the electric field intensities of the scattered wave and incident electromagnetic wave, respectively.

3 Results and discussion

Figure S1(a) in the Electronic Supplementary Material (ESM) shows the XRD patterns of the FeCo-PBA before and after etching, where both the nanocube and etched nanocage exhibit a typical PBA-type diffraction pattern corresponding to the face-centered cubic structure [35]. Notably, the diffraction peaks of etched FeCo-PBA nanocages shift slightly toward high-angle, which may be attributed to partial ion dissolution in HCl and consequent lattice shrinking. The SEM images of FeCo-PBA present uniform nanocube morphology before etching with particle sizes of 273.2 ± 35.9 nm (Fig. S1(b) in the ESM), while the etching treatment gives rise to hollow nanocage morphology with surface cracks and pores (Fig. S1(c) in the ESM). Insufficient amount of etching agent would

清华大学出版社 Tsinghua University Press | SciOpen

lead to only rough surface of FeCo-PBA nanocubes (Fig. S2(a) in the ESM), while excessive etching agent resulted in severely distorted edges and even collapse of nanocages (Fig. S2(b) in the ESM). TEM images taken from the FeCo-PBA nanocages (Fig. S3 in the ESM) reveal the distinct contrast between the interior and exterior regions, further demonstrating the hollow structure after etching treatment. ICP-OES has been conducted to determine the metallic element proportion of the FeCo-PBA nanocages, resulting in Fe:Co atomic ratio of 1.986:3.061 that matches well with the nominal composition of the $Co_3[Fe(CN)_6]_2$ reactants.

Figure S4 in the ESM shows the XRD patterns of the FeCo-PBA nanocages after annealing in air (S1) and thermal reduction (S2–S4). The broad peaks of S1 are composed of two similar sets of XRD standard patterns $CoFe_2O_4$ (JCPDS Card No. 03-0864) and Co_3O_4 (JCPDS Card No. 43-1003). The emergence of ferrimagnetic $CoFe_2O_4$ semiconductor arises from mutual diffusion andoxidation of Fe and Co atoms during air annealing, which drives the formation of an inverse spinel ferrite structure. Due to the relatively high Co content in the pristine FeCo-PBA, the residual Co atoms are further oxidized to antimagnetic Co_3O_4 semiconductor with spinel structure. For the S2 and S3, additional peaks at 44.9°, 65.3°, and 82.7° have been observed, corresponding to the (110), (110), (200), and (211) planes of the FeCo alloy (JCPDS Card No. 49-1568). Notably, the diffraction peaks of Co_3O_4 disappear in the S2, indicating the preferential reduction of Co_3O_4 during thermal treatment. In contrast, the peaks of $CoFe_2O_4$ persist in the S2 and S3 and only disappear completely in the S4. Such discrepancy in reduction kinetics can be attributed to higher stability of the inverse spinel structure with Fe^{3+} occupying octahedral sites. The grain sizes of FeCo have been calculated using the Scherrer Formula, resulting in 21.44, 31.28, and 38.05 nm for the S2, S3, and S4, respectively. The increased grain size is assigned to prolonged thermal reduction time which provides sufficient energy for grain growth. Benefitted from multi-step thermal reduction process, the pristine $CoFe_2O_4$ in nanocages can serve as steric hindrance to constrain the rapid growth of FeCo nanoparticles at the initial stage, giving rise to the confined grain size and dispersed distribution in the S2.

SEM images in Figs. 1(a)–1(d) show the morphology of the S1–S4 after annealing treatment. The S1 exhibits similar architecture to the etched FeCo-PBA nanocages (Fig. S1(c) in the ESM), with a size of 267.4 ± 37.8 nm (Fig. 1(a)). The cubic structure has been largely maintained due to near-equivalent substitution of C or N elements with oxygen during oxidation annealing. For the S2, thermal reduction transforms the continuous surfaces into a porous network composed of conterminous nanoparticles with a size of 34.7 ± 5.2 nm (Fig. 1(b)). The confinement effect of $CoFe_2O_4$ within nanocage framework inhibits the excessive growth of FeCo nanoparticles, giving rise to small particle sizes close to the quasi-single-domain range (20–30 nm). Distinct volume shrinkage has also been observed in the S2, reducing the cubic size to ~ 249.1 ± 43.5 nm due to oxygen dissociation from FeCo oxides during the reduction process. Further extended annealing duration leads to collapsed cubic architecture in the S3, with particle agglomeration and increased size of 56.2 ± 7.4 nm (Fig. 1(c)). For the S4 (Fig. 1(d)), the cubic morphology degrades entirely into severe agglomeration of large FeCo particles with a size of 91.5 ± 13.6 nm.

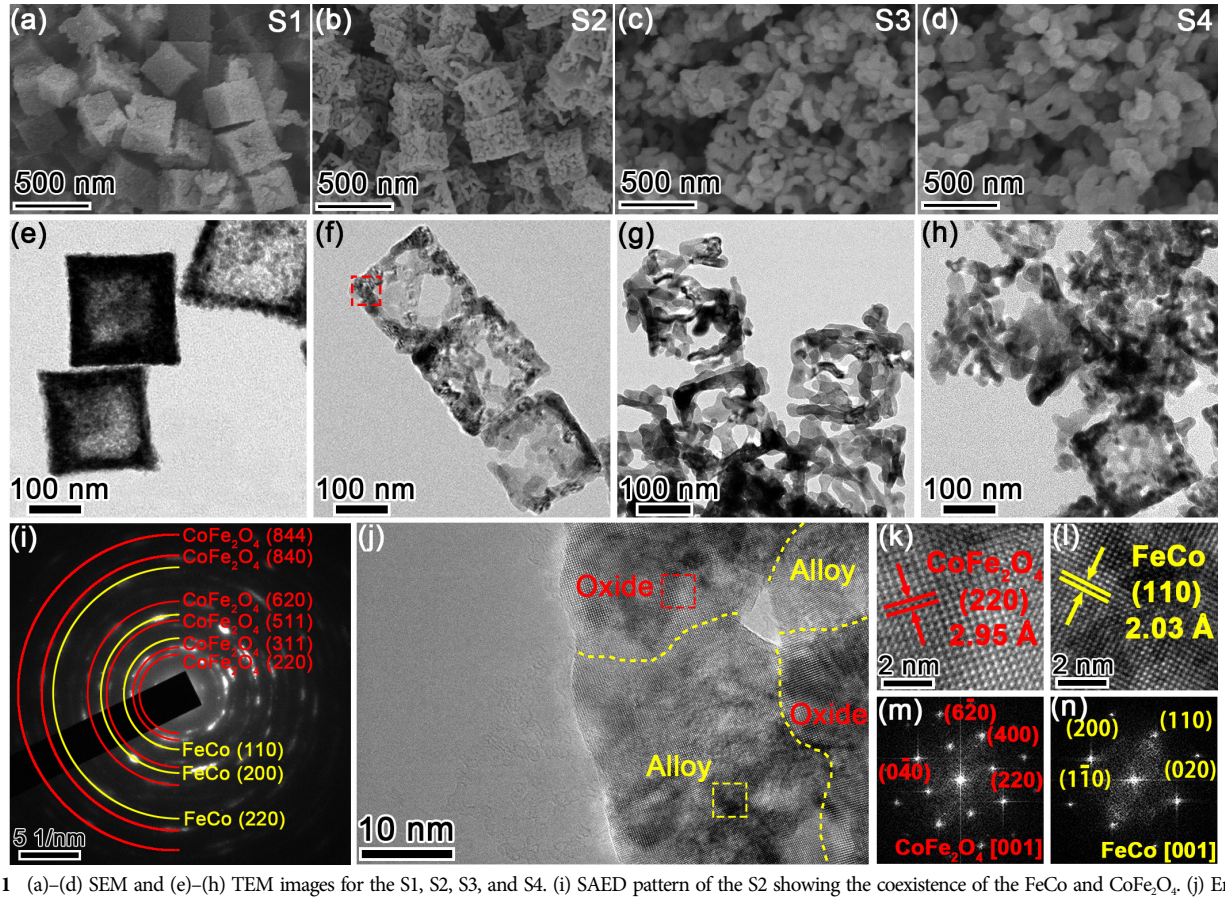


Figure 1 (a)–(d) SEM and (e)–(h) TEM images for the S1, S2, S3, and S4. (i) SAED pattern of the S2 showing the coexistence of the FeCo and $CoFe_2O_4$. (j) Enlarged TEM image of the S2 taken from the red region in (f). (k) and (l) HRTEM images and ((m) and (n)) corresponding FFT diffraction patterns taken from red and yellow regions in (j) respectively.

Figures 1(e)–1(n) present the TEM images of S1–S4 to reveal the detailed microstructures. The S1 exhibits cubic shape with a bright interior and dark edge, demonstrating the maintained hollow feature (Fig. 1(e)). For the S2 (Fig. 1(f)), the hollow structure become more evident due to the presence of surface pores, while the cubic framework remains recognizable. In contrast, the cubic structure of the S3 almost collapses and adjacent particles have interconnected to each other to form chain-like structures (Fig. 1(g)). The S4 exhibits no detectable cubic feature, with severe particle aggregation observed (Fig. 1(h)). Since the S2 nanocage maintains the hollow feature, which maybe facilitate the multiple EM scattering and impedance matching [36], the detailed microstructure and composition of the S2 has been further investigated. Figure 1(i) shows the SAED pattern taken from the S2 nanocage, demonstrating the formation of FeCo and $CoFe_2O_4$. Figure 1(j) presents high resolution TEM (HRTEM) image from the edge of the nanocage indicated by the red regtangle in Fig. 1(f). The lattice spacings of 2.95 Å (Fig. 1(k)) and 2.03 Å (Fig. 1(l)) have been measured, corresponding to the $CoFe_2O_4$ (220) plane and FeCo (110) plane. The fast Fourier transformation (FFT) diffraction patterns (Figs. 1(m) and 1(n)) have also been conducted in the red and yellow region in Fig. 1(k), further confirming the coexistence of FeCo and $CoFe_2O_4$ phases in the S2.

To investigate the EM wave absorption ability, EM parameters and the loss tangent of the S1–S4 have been investigated. Figures 2(a) and 2(b) show increased real permittivity (ε') and imaginary permittivity (ε'') from the S1 to the S4, which can be attributed to raised FeCo content with strong conductive and dielectric properties. The dielectric loss tangent ($\tan\delta_\varepsilon = \varepsilon''/\varepsilon'$, Fig. 2(c)) represents the dielectric dissipation ability of the incident EM wave, indicating that the S1 exhibits two dielectric loss peaks located in 2.00–4.70 and 9.30–18.00 GHz with the peak values of 0.04 and 0.11. For the S2, similar dual peak feature and larger peak intensities of 0.09 and 0.18 have been observed, with a broader peak width of 8.40–18.00 GHz. The S3 presents single extra-broad loss peak with peak value of 0.23 located in 5.40–18.00 GHz, while a narrower (4.70–16.30 GHz) but stronger (0.40) peak appears in the S4. Overall, the dielectric loss peak intensity for the S1–S4 exhibits an increasing trend, while the peak frequency shifts to lower frequency with raised FeCo content. For the dynamic magnetic properties (Figs. 2(d) and 2(e)), the real permeability (μ') and imaginary permeability (μ'') increase from the S1 to S3, followed by declining for the S4. The magnetic loss tangent ($\tan\delta_m = \mu''/\mu'$) of the S1 exhibit a broad loss peak with the value of 0.16 located in 7.10–15.80 GHz (Fig. 2(f)). For the S2, a single loss peak with larger intensity of 0.54 has been obtained between 10.30 and 18.00 GHz. The S3 and S4 exhibit a similar peak to the S2 with a lower intensity of 0.41 and 0.27, respectively. The peak frequency of the tan δ_m increases from 12.32 GHz (S1) to 15.44 GHz (S2) and 15.84 GHz (S3), prior to decreasing to 13.76 GHz for the S4 (Fig. 2(f)).

Based on the transmission line theory [37], the RL has been calculated from the measured relative complex permittivity and permeability according to the following equations [38, 39]

$$RL = 20\lg\frac{|Z_{in}-1|}{|Z_{in}+1|} \quad (2)$$

$$Z_{in} = \sqrt{\frac{\mu_r}{\varepsilon_r}}\tanh\left(j\frac{2\pi fd}{c}\sqrt{\mu_r\varepsilon_r}\right) \quad (3)$$

where c is the velocity of light, d is the thickness of the absorber, f is the frequency, j is the imaginary root, Z_{in} is the normalized input impedance of the absorber. The S1 exhibit poor RL peak of −7.3 dB at a thickness of 3.7 mm (Figs. 3(a) and 3(e)) while the S2 exhibit superior absorption of −47.4 dB and broad effective absorption bandwidth (EAB, RL < −10 dB) of 7.10 GHz at a small thickness of 1.9 mm (Figs. 3(b) and 3(f)). Additionally, at a smaller thickness of 1.6 mm, the S2 achieves broad EAB of 5.91 GHz and a minimum RL of −25.1 dB (Fig. 3(f)). For the S3, the minimum RL of −45.4 dB has been obtained at a thickness of 1.6 mm and the widest EAB of 6.92 GHz is achieved at a thickness of 1.2 mm (Figs. 3(c) and 3(g)). For the S4 composed of pure FeCo phase, the minimum RL deteriorates to −31.1 dB at a large thickness of 2.9 mm, and the EAB also decreases to 2.72 GHz at a thickness of 1.0 mm (Figs. 3(d) and 3(h)).

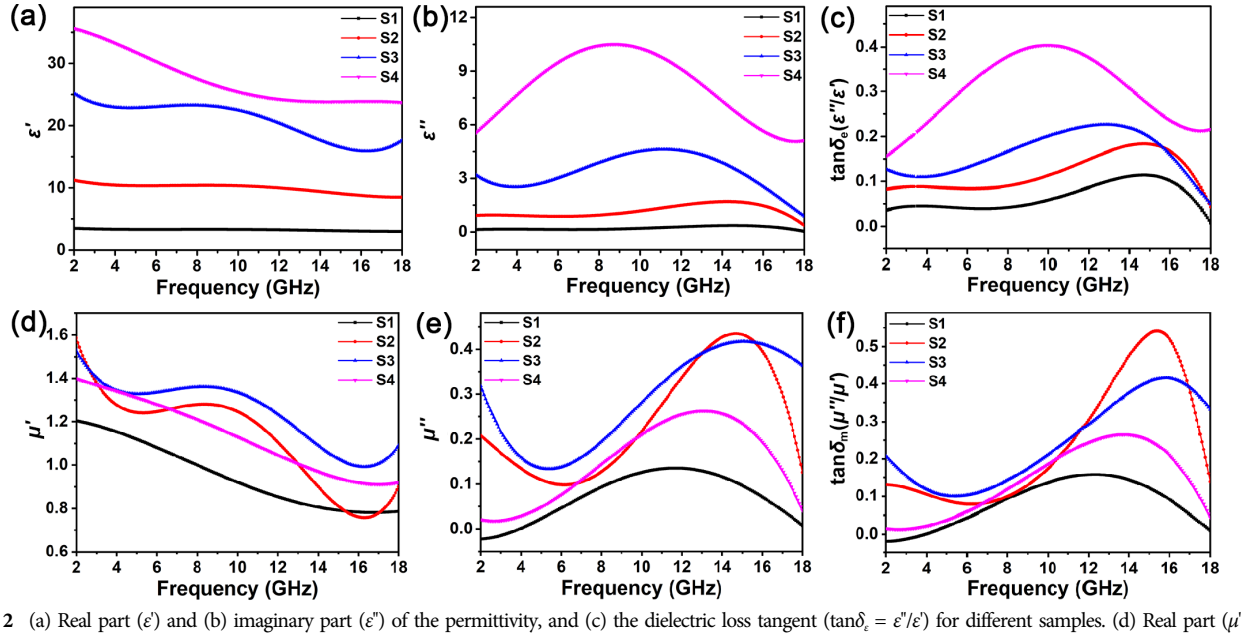


Figure 2 (a) Real part (ε') and (b) imaginary part (ε'') of the permittivity, and (c) the dielectric loss tangent ($\tan\delta_\varepsilon = \varepsilon''/\varepsilon'$) for different samples. (d) Real part (μ') and (e) imaginary part (μ'') of the permittivity, and (f) the magnetic loss tangent ($\tan\delta_m = \mu''/\mu'$) for different samples.

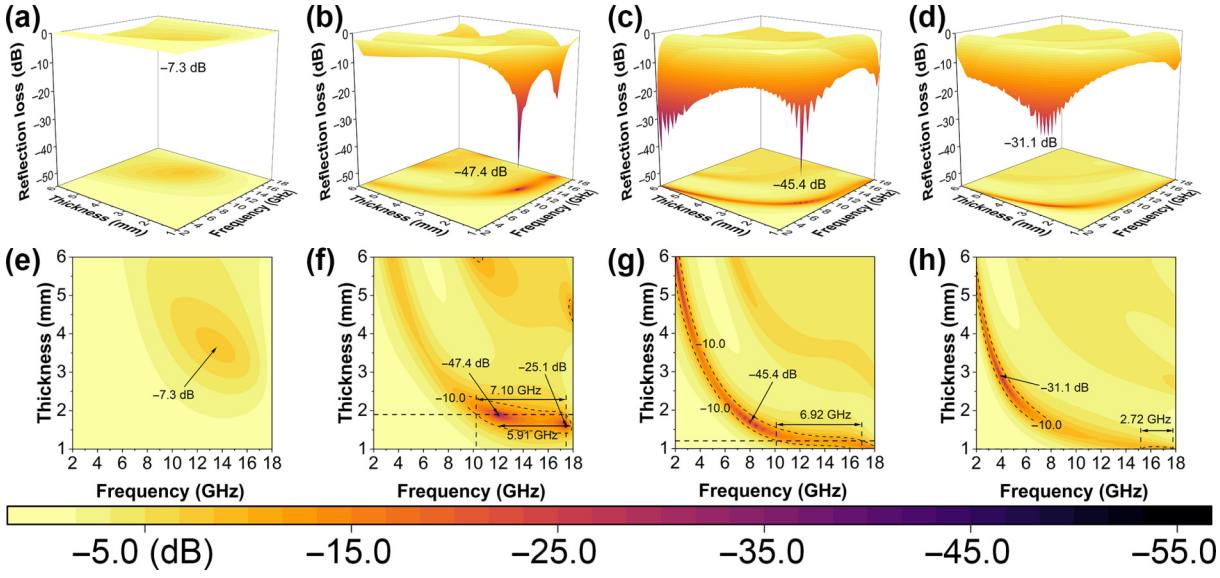


Figure 3 (a)–(d) 3D representations of RL and (e)–(h) corresponding projection mapping for the S1–S4.

In order to reveal the practical applications of absorbers in real space, CST Studio has been employed to simulate the electromagnetic wave absorption performance and the 3D RCS. The simulation model is composed of the actual composites under investigation and a PEC. The intensity of the reflected signal from the pure PEC and S1–S4 coating was tracked under the condition of vertically incident electromagnetic waves, with measurements taken over the full detection angle. The corresponding simulation thickness and frequency are 3.7 mm and 13.4 GHz (S1), 1.9 mm and 12.0 GHz (S2), 1.6 mm and 8.0 GHz (S3), 2.9 mm and 4.16 GHz (S4), respectively. Figures 4(a)–4(e) show the simulated 3D RCS for the PEC and S1–S4, where the intensity of RCS reflection can be assessed by the depth of the colors in the 3D images, and the Theta and Phi represent the incident angle and polarization angle of the plane wave, respectively. The pure PEC reflects all the incident electromagnetic waves, while the S2 and S3 exhibit the weak reflection intensity, demonstrating the enhanced EM wave absorbing performance for the S2 and S3. Additionally, two-dimensional (2D) RCS across various detection angles have been plotted to reveal the RCS reflection intensity of the PEC and S1–S4 at an incident wave angle of 0° (Fig. 4(f)). Compared to the PEC and S1, the S2, S3, and S4 show significantly decreased reflection intensity, with low RCS values below −20 dB·m^2 over a wide angular range from −60° to 60°. Notably, compared to the pure PEC, the RCS value of the S3 is significantly reduced by 34.6 dB·m^2 at 0°, exhibiting the minimal EM reflection. At other angles (Figs. 4(g)–4(k)), the RCS reflection intensity of the S2 and S3 are similar but higher than that of S4, indicating that both S2 and S3 possess superior EM attenuation capability in real space to effectively mitigate EM scattering and reflection.

To further analyze the dielectric loss, the Cole–Cole curves have been depicted in Figs. 5(a)–5(d). According to the Debye equation [40], the complex permittivity of a dielectric material can be expressed as follows

$$\varepsilon' = \varepsilon_\infty + \frac{\varepsilon_s - \varepsilon_\infty}{1+\omega^2\tau^2} \tag{4}$$

$$\varepsilon'' = \frac{\varepsilon_s - \varepsilon_\infty}{1+\omega^2\tau^2}\omega\tau + \frac{\sigma}{\omega\varepsilon_0} \tag{5}$$

where ω is the angular frequency, τ is the relaxation time, ε_s is the static dielectric constant, ε_∞ is the optical dielectric constant, ε_0 is the dielectric constant in vacuum respectively and σ is the conductivity. Based on Eqs. (4) and (5), the relationship between ε' and ε'' without consideration of the σ can be deduced

$$\left(\varepsilon' - \frac{\varepsilon_s + \varepsilon_\infty}{2}\right)^2 + (\varepsilon'')^2 = \left(\frac{\varepsilon_s - \varepsilon_\infty}{2}\right)^2 \tag{6}$$

Such relationship indicates that if dielectric loss arises from a relaxation process, a semicircle emerges in the Cole–Cole curve, with each semicircle corresponding to a Debye relaxation process. For the S1 (Fig. 5(a)), two distinct semicircles are observed in the Cole-Cole curves, which can be assigned to the loss peaks located at 2.00–4.70 and 9.30–18.00 GHz (Fig. 2(c)). The small oxide particles within nanocages tend to form massive defects such as vacancies in the lattice and dangling bonds on the surface, which may serve as orientation polarization sites of dipoles [41]. Hence these two dielectric relaxation processes correspond to the orientation polarization relaxation of the $CoFe_2O_4$ and the Co_3O_4 respectively. The Cole–Cole curve of the S2 also exhibits two semicircles while the left one is larger than that of the S1 (Fig. 5(b)). Since the thermal reduction leads to formation of FeCo phase within S2, the different dielectric properties between the highly conductive FeCo phase and semiconducting $CoFe_2O_4$ may generate abundant heterogeneous interfaces for improved interfacial polarization. Previous work reported that the peak frequency of the interfacial polarization between FeCo and $CoFe_2O_4$ is located at 10.20–15.50 GHz [42], consistent with our observations here. Hence, the peak of FeCo/$CoFe_2O_4$ interfacial polarization partially overlaps with the dipole polarization peak of the oxides, leading to the broader width (8.40–18.00 GHz) andhigher value of the second loss peak in the S2 (Fig. 2(c)). For the S3, a single larger semicircle (Fig. 5(c)) corresponds to the broad loss peak between 5.40 GHz and 18.00 GHz (Fig. 2(c)), indicating superposition of dipole polarization from the oxides and stronger interfacial polarization at FeCo/$CoFe_2O_4$ interfaces. The S4 composed of pure FeCo phase exhibits a narrower semicircle (Fig. 5(d)) corresponding to the loss peak in 4.70-16.30 GHz (Fig. 2(c)), attributed to the interfacial polarization between the FeCo and paraffin matrix. Furthermore,

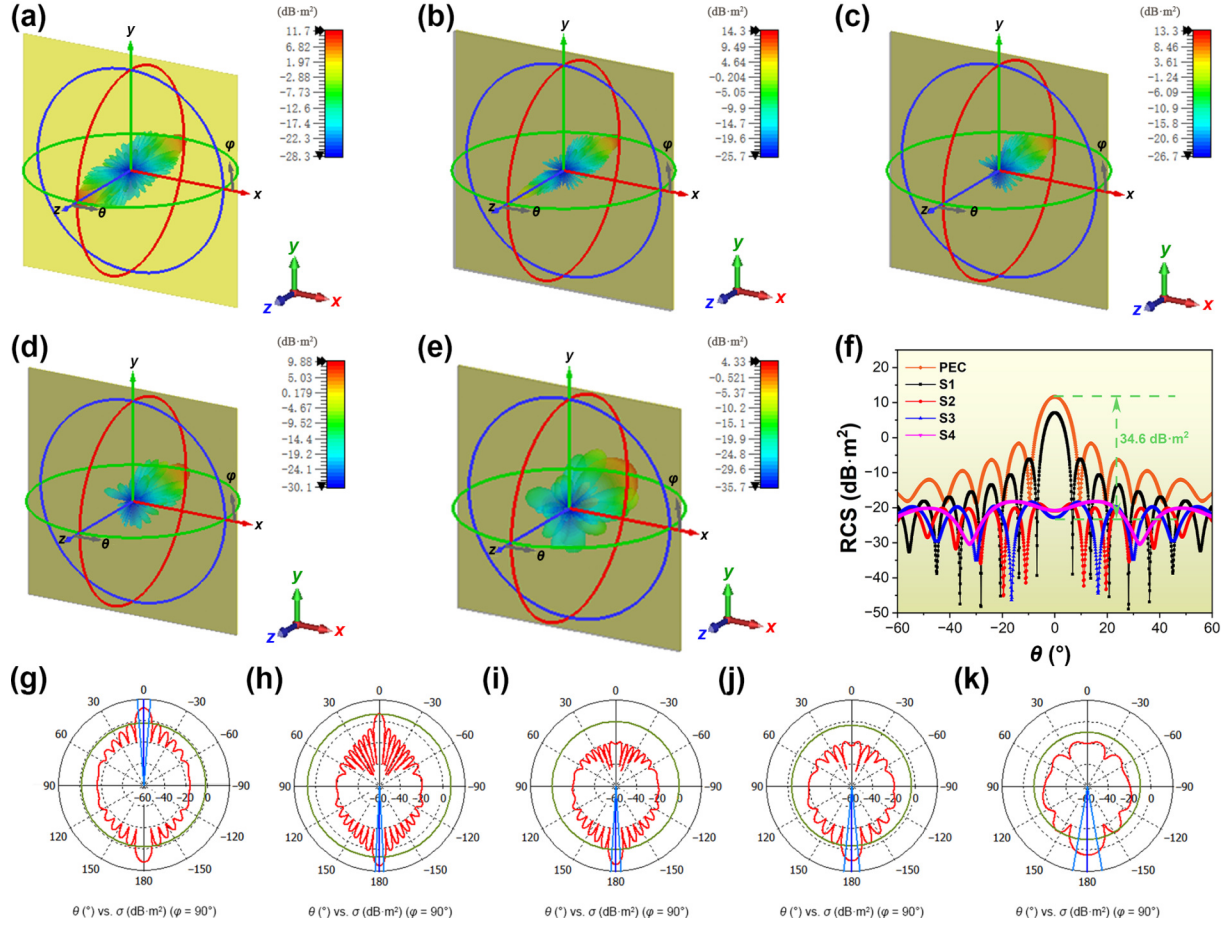


Figure 4 3D RCS simulations for the (a) PEC and (b)–(e) S1–S4, where θ and φ represent the incident angle and polarization angle of the plane wave, respectively. (f) Comparison of 2D RCS values at various detection angles. RCS values across the entire detection angle for the (g) PEC and (h)–(k) S1–S4.

based on the reported method [43, 44], the imaginary part of the permittivity was deconvoluted to assess the respective contributions of polarization and conduction losses. The analysis reveals that polarization loss is dominant in the FeCo composite nanocages (samples S2 and S3), whereas conduction loss is comparatively minor (Fig. S5 in the ESM). This weaker conduction loss can likely be attributed to the random and incomplete electrical connections among the FeCo composite particles.

The magnetic loss in the GHz range primarily involves magnetic resonance loss and eddy current loss. The magnetic resonance comprises natural resonance and exchange resonance, which can be described by the following equation deduced by Kittel and Aharoni [45, 46]

$$f = \frac{\gamma_0}{2\pi}\left(H_A + \frac{C\mu_{kn}^2}{R^2 M_s}\right) \quad (7)$$

where γ_0 is the gyromagnetic ratio, H_A is the magnetic anisotropy field, C is the exchange constant, μ_{kn} is the root of spherical Bessel function, R is the radius of the nanoparticle and M_s is the saturation magnetization. The f corresponding to the natural and exchange resonance is related to the first part and the second of Eq. (7), respectively. Based on Eq. (7), the natural resonance frequency is directly proportional to the magnetic anisotropy field, which can be reflected by the coercivity. Consequently, the static magnetic properties of the S1, S2, S3, and S4 have been measured in Figs. 5(e) and 5(f). The S1 composed of $CoFe_2O_4$ and Co_3O_4 presents the lowest M_s of 23.2 emu/g since the $CoFe_2O_4$ and Co_3O_4 exhibit ferrimagnetic and antiferromagnetic feature at room temperature respectively [47], with magnetism significantly weaker than that of ferromagnetic materials. With raised thermal reduction time, the S2, S3, and S4 exhibit increased M_s values of 55.8, 148.3, and 178.6 emu/g due to higher intrinsic M_s of FeCo alloy compared with FeCo oxides [48]. The coercivity (H_c) exhibits anincreasing trend initially with the value of 390.6, 766.8, and 970.1 Oe for the S1, S2, and S3 followed by a decrease to 576.0 Oe for the S4. Since the S1 consists of antiferromagnetic Co_3O_4 and ferrimagnetic $CoFe_2O_4$ phases, the coercivity of 390.0 Oe is determined by the $CoFe_2O_4$ phase. For the S2 and S3, oxide phases have been partially converted to ferromagnetic FeCo phase with harder magnetism [49], giving rise to larger coercivity than the S1. Notably, the S4 with pure FeCo phase presents lower coercivity than that of the S3. Such evolution of coercivity can be attributed to the extrinsic magnetic feature which not only depends on phase composition but also the surface anisotropy related to particle size [50]. For submicrometer particles, $K_{eff} = K_V' + 6K_S'/d$, where K_{eff} is the effective anisotropy constant, K_V' and K_S' are the volume and surface anisotropy energy constants, and d is the diameter of the particles [51–53]. The particle size within S2–S4 increases from 34.7 ± 5.2 to 56.2 ± 7.4 and 91.5 ± 13.6 nm (Figs. 1(c)–1(e)), leading to gradually decreasing surface anisotropy and smaller coercivity of the S4. The peak frequencies of the natural resonance peaks for the S1–S4 are located at 12.32, 15.44, 15.84, and 13.76 GHz (Fig. 2(f)), with similar variation trend to the change of the H_c.

The natural resonance peak intensity of the S1, S2, S3, and S4

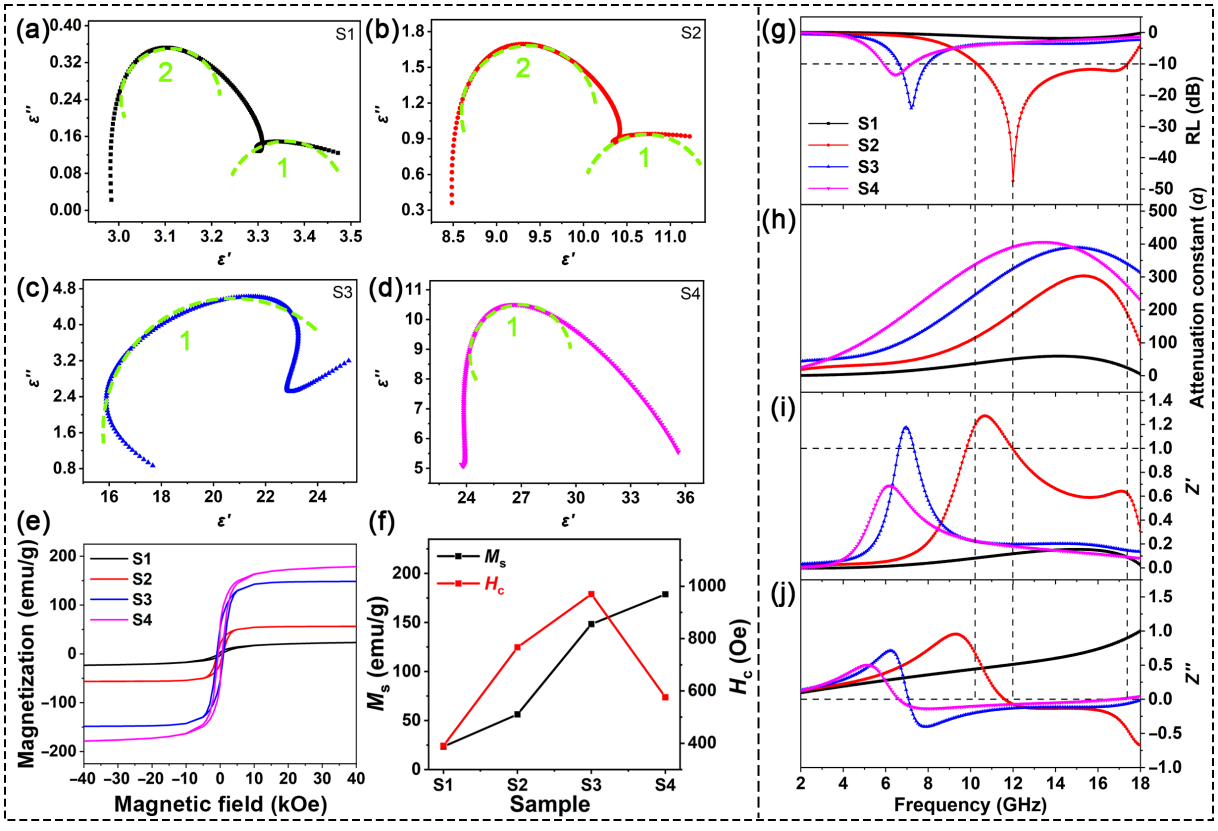


Figure 5 Cole–Cole curves plotted for the (a) S1, (b) S2, (c) S3, and (d) S4. (e) Hysteresis loops and (f) detailed M_s as well as H_c of the S1–S4. (g) RL, (h) attenuation constant (α), (i) real part (Z'), and (j) imaginary part (Z'') of the normalized input impedance at the same thickness of 1.90 mm for the S1–S4.

increases firstly and then presents a decreasing trend (Fig. 2(f)), which can be ascribed to competition effect of the phase composition evolution and variation in the particle size. The S1 is composed of antiferromagnetic Co_3O_4 and ferrimagnetic $CoFe_2O_4$ phase, hence exhibiting the lowest loss peak. In the S2, the antiferromagnetic Co_3O_4 has been preferentially transformed into the FeCo phase with large saturation magnetization. The dispersive distribution of the FeCo and oxides with small particle size gives rise to enhanced magnetic anisotropy and natural resonance loss. For the S3 and S4, reduced oxide content together with increased particle size facilitate contacts between FeCo particles, coherently leading to large overall conductivity as shown in Fig. S6 in the ESM. Consequently, the incident EM wave tends to induce large eddy current on the absorber surface, giving rise to lower natural resonance loss. Figure S7 in the ESM shows the eddy current coefficients (C_0) for all the samples, where the S3 and S4 present flatter curves in broad frequency range of 5.10–18.00 GHz than the S2, demonstrating the enhanced eddy current loss in the S3 and S4. The less penetration of EM wave for the S3 and S4 than the S2 can also be reflected in the impedance matching condition. Figures 5(g)–5(j) present the curves of RL, attenuation constant, real part (Z') and imaginary part (Z'') of the normalized input impedance at the same thickness of 1.9 mm. Despite the strongest attenuation in the S4 due to increased FeCo content, the S2 achieves superior impedance matching over a wide frequencyrange with Z' and Z'' approaching 1 and 0, respectively, allowing the maximum EM wave to enter into the absorber for efficient attenuation and optimal absorbing capability (Figs. 5(i) and 5(j)). Besides, the FeCo magnetoelectric composite nanocages (sample S2 and S3) exhibits both favorable magnetic and dielectric losses with moderate ratio over the whole investigated frequency range (Fig. S8 in the ESM), which not only contributes to multiple effective loss mechanisms but also promotes impedance matching.

Figure 6(a) illustrates the mechanisms involved in the EM wave absorption of the FeCo magnetoelectric composite nanocages. The uniform distribution of FeCo nanoparticles among oxide matrix ensures satisfactory impedance matching, allowing maximum entrance of EM wave. The hollow structure together with porous surface favor multiple scattering of incident wave for enhanced dissipation. As both of the FeCo and $CoFe_2O_4$ are magnetic phases, which avoids the magnetic dilution effect and facilitates larger magnetic loss. The magnetic particles and oxide particles confine with each other for small particle size, giving rise to improved natural resonance loss and absorbing frequency. Last but not the least, the alloy/oxide nano-heterostructure generates multiple sites for interfacial polarization, and nanoparticles with dangling bonds on the surface contributes to dipole polarization, which together constitute enhanced dielectric loss. Consequently, compared to other related material systems (Fig. 6(b) and Table S1 in the ESM), the FeCo composite hollow nanocages in this work achieve strong absorption of −47.4 dB and broad bandwidth of 7.10 GHz at a small thickness of 1.9 mm (Fig. 6(b)), exhibiting superior comprehensive EM absorbing performance.

4 Conclusions

In summary, hollow FeCo magnetoelectric composite nanocages have been prepared via controlled etching and annealing treatment of FeCo-PBA precursors. Benefitted from confinement effect of ferrimagnetic $CoFe_2O_4$, well-dispersed ferromagnetic FeCo nanoparticles with quasi-single-domain size have been obtained,

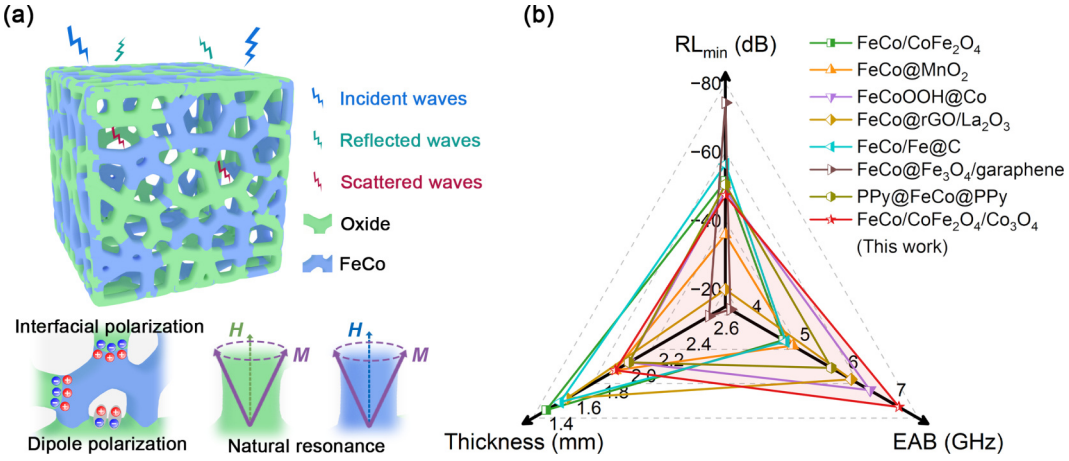


Figure 6 (a) EM loss mechanisms for the enhanced EM absorption in the FeCo magnetoelectric composite nanocages. (b) Comparison of EAB, thickness, and RL_{min} for the EM wave absorption performance of the FeCo composite hollow nanocages with other related material systems.

giving rise to enhanced magnetic anisotropy and high-frequency natural resonance. Multiple heterogeneous interfaces and large surface area of the nanocages contribute to intensified dielectric loss including interfacial polarization and dipole polarization as well as conductive loss. Rational ratio and distribution of constituent FeCo alloy and $CoFe_2O_4$ semiconductor with hollow and porous structure facilitate satisfactory impedance matching for maximum EM wave incidence. Consequently, the magnetoelectric composite nanocages exhibit exceptional EM wave absorption performance with RL of −47.4 dB and broad EAB of 7.10 GHz at a small thickness of 1.9 mm. This work not only realizes efficient and wideband EM absorption but also provides a versatile confinement strategy to design hierarchical nanocomposites for extended electromagnetic applications.

Electronic Supplementary Material: Supplementary material (XRD, SEM, TEM, electrical conductivity and eddy current criteria C_0 data) is available in the online version of this article at https://doi.org/10.26599/NR.2026.94908356.

Data availability

All data needed to support the conclusions in the paper are presented in the manuscript and the Electronic Supplementary Material. Additional data related to this paper may be requested from the corresponding author upon request.

Acknowledgements

This work was supported by the National Natural Science Foundation of China (Nos. 52122106 and 52401302) and the "Pioneer" R&D Program of Zhejiang Province (No. 2023C01076).

Declaration of competing interest

All the contributing authors report no conflict of interests in this work.

Author contribution statement

H. P. L.: Data curation, validation, writing manuscript, experimental design. P. B. Z.: Data curation, experimental design. J. T.: Writing manuscript, experimental design. M. Y.: Project administration, funding acquisition. G. L.: Project administration, funding acquisition, writing manuscript. C. W.: Project administration, funding acquisition, writing manuscript. All the authors have approved the final manuscript.

Use of AI statement

None.

References

[1] Li, X. F.; Chen, C. Y.; Li, Z. Y.; Yi, P.; Zou, H. H.; Deng, G.; Fang, M.; He, J. Z.; Sun, X.; Yu, R. H. et al. Inter-skeleton conductive routes tuning multifunctional conductive foam for electromagnetic interference shielding, sensing and thermal management. *Nano-Micro Lett.* **2025**, *17*, 52.

[2] Pan, F.; Shi, Y. Y.; Yang, Y.; Guo, H. T.; Li, L. X.; Jiang, H. J.; Wang, X.; Zeng, Z. H.; Lu, W. Porifera-inspired lightweight, thin, wrinkle-resistance, and multifunctional MXene foam. *Adv. Mater.* **2024**, *36*, 2311135.

[3] Wu, L. H.; Liu, J.; Liu, X.; Mou, P. P.; Lv, H. M.; Liu, R.; Wen, J. G.; Zhao, J. C.; Li, J. L.; Wang, G. Z. Microwave-absorbing foams with adjustable absorption frequency and structural coloration. *Nano Lett.* **2024**, *24*, 3369–3377.

[4] Zhao, Z. H.; Qing, Y.; Kong, L.; Xu, H. L.; Fan, X. M.; Yun, J. J.; Zhang, L. M.; Wu, H. J. Advancements in microwave absorption motivated by interdisciplinary research. *Adv. Mater.* **2024**, *36*, 2304182.

[5] Liu, C. Y.; He, T. A.; Hu, C. C.; Qian, Q.; Hao, Y. L.; Xu, L.; Lu, H. Y.; Ji, G. B. The optimized design of sandwich structured SiO_2/C@SiC/SiO_2 composites through numerical simulation for temperature-resistant radar and infrared compatible stealth. *Adv. Funct. Mater.* **2025**, *35*, 2416108.

[6] Zhang, Y. H.; Zhang, L.; Si, H. X.; Zhang, Y.; Li, C. P.; Zhang, L.; Zhang, J. W.; Gong, C. H. TiN nanofiber metacomposites for efficient electromagnetic wave absorption: Insights on multiple reflections and scattering effects. *J. Mater. Sci. Technol.* **2025**, *233*, 69–79.

[7] Xiao, J. X.; Zhan, B. B.; He, M. K.; Qi, X. S.; Zhang, Y. L.; Guo, H.; Qu, Y. P.; Zhong, W.; Gu, J. W. Mechanically robust and thermal insulating nanofiber elastomer for hydrophobic, corrosion-resistant, and flexible multifunctional electromagnetic wave absorbers. *Adv. Funct. Mater.* **2025**, *35*, 2419266.

[8] Sun, R.; Lv, H. W.; Lian, G. J.; Wang, L.; Huang, M. Q.; You, W. B.; Che, R. C. Dielectric shell regulation in synergy FeCoNi@$ZnIn_2S_4$ microspheres with broadband electromagnetic wave absorption. *Soft*

Sci. **2025**, *5*, 35.

[9] Zhou, H. W.; Lin, Y.; Ma, Y. Z.; Han, L. Y.; Cai, Z. X.; Cheng, Y.; Yuan, Q. B.; Huang, W. H.; Yang, H. B.; Che, R. C. Hierarchical structure Fe@CNFs@Co/C elastic aerogels with intelligent electromagnetic wave absorption. *InfoMat* **2025**, *7*, e12630.

[10] Guo, Y. Q.; Li, P.; Zhao, R. L.; Gu, J. W. Preparation and mechanism of thermally conductive polyimide phase change composites with electromagnetic wave-absorbing performance. *Acta Polym. Sin.*, in press, DOI: 10.11777/j.issn1000-3304.2025.25144.

[11] Fan, X. X.; Zhang, X. C.; Li, L.; Cao, M. S. Recent progress and perspective of microwave absorption materials derived from metal-organic frameworks. *Soft Sci.* **2024**, *4*, 43.

[12] Yao, L.; Dang, J.; Xiao, J. X.; Chen, Y. L.; Ding, J. F.; Qu, Y. P.; Peng, Q.; Qi, X. S.; Zhong, W. Metal chelate-derived and catalytical strategy to produce CoFe/C@bamboo-like carbon nanotubes for microwave absorption, hydrophobicity, and corrosion resistance. *J. Mater. Sci. Technol.* **2026**, *240*, 190–200.

[13] Wang, H. M.; Xiao, J. X.; Qi, X. S.; Gong, X.; Ding, J. F.; Qu, Y. P.; Yang, J. L.; Zhong, W. Microstructural optimization and non-metallic doping strategy to develop mesoporous N-doped carbon hollow nanospheres for strong and broadband microwave absorption. *J. Mater. Sci. Technol.* **2026**, *247*, 55–63.

[14] Cao, X. L.; Jia, Z. R.; Hu, D. Q.; Wu, G. L. Synergistic construction of three-dimensional conductive network and double heterointerface polarization via magnetic FeNi for broadband microwave absorption. *Adv. Compos. Hybrid Mater.* **2022**, *5*, 1030–1043.

[15] Guan, G. G.; Yan, L.; Zhou, Y. T.; Xiang, J.; Gao, G. J.; Zhang, H. Y.; Gai, Z. Q.; Zhang, K. Y. Composition design and performance regulation of three-dimensional interconnected FeNi@carbon nanofibers as ultra-lightweight and high efficiency electromagnetic wave absorbers. *Carbon* **2022**, *197*, 494–507.

[16] Li, C.; Qi, X. S.; Gong, X.; Peng, Q.; Chen, Y. L.; Xie, R.; Zhong, W. Magnetic-dielectric synergy and interfacial engineering to design yolk-shell structured CoNi@void@C and CoNi@void@C@MoS_2 nanocomposites with tunable and strong wideband microwave absorption. *Nano Res.* **2022**, *15*, 6761–6771.

[17] Liu, A.; Xu, X. S.; Qiu, H.; Guo, H.; He, M. K.; Yu, Z.; Zhang, Y. L.; Gu, J. W. Bioinspired hollow heterostructure fillers for enhanced electromagnetic interference shielding in polyimide aerogels. *InfoMat* **2025**, *7*, e70060.

[18] Qi, J. M.; Liang, C. B.; Ruan, K. P.; Li, M. K.; Guo, H.; He, M. K.; Qiu, H.; Guo, Y. Q.; Gu, J. W. Cactus-like architecture for synergistic microwave absorption and thermal management. *Natl. Sci. Rev.* **2025**, *12*, nwaf394.

[19] Zhou, L.; Hu, P. F.; Bai, M.; Leng, N.; Cai, B.; Peng, H. L.; Zhao, P. Y.; Guo, Y. Q.; He, M. K.; Wang, G. S. et al. Harnessing the electronic spin states of single atoms for precise electromagnetic modulation. *Adv. Mater.* **2025**, *37*, 2418321.

[20] Gong, X. F.; Xiang, L. L.; Qi, X. S.; Gong, X.; Chen, Y. L.; Peng, Q.; Qu, Y. P.; Wu, F. Z.; Sun, K.; Zhong, W. Improved polarization loss and impedance matching induced by carbon paper-based magnetic heterostructured composites for lightweight and strong microwave absorption. *Adv. Compos. Hybrid Mater.* **2024**, *7*, 216.

[21] Cui, X. J.; Jiang, Q. R.; Wang, C. S.; Wang, S. H.; Jiang, Z. Y.; Li, X. A.; Deng, D. H. Encapsulating FeCo alloys by single layer graphene to enhance microwave absorption performance. *Mater. Today Nano* **2021**, *16*, 100138.

[22] Zhang, H.; Zhao, Y. P.; Yuan, M. Y.; Sun, C.; Huang, H.; Jiang, Y. C.; Fan, Z.; Che, R. C.; Pan, L. J. Construction of chiral magnetic structure with enhancement in magnetic coupling for efficient Low-Frequency microwave absorption. *Chem. Eng. J.* **2024**, *493*, 152692.

[23] He, M. K.; Hu, J. W.; Yan, H.; Zhong, X.; Zhang, Y. L.; Liu, P. B.; Kong, J.; Gu, J. W. Shape anisotropic chain-like CoNi/polydimethylsiloxane composite films with excellent low-frequency microwave absorption and high thermal conductivity. *Adv. Funct. Mater.* **2025**, *35*, 2316691.

[24] Zhang, Y.; Wang, X. W.; Dong, T.; Yang, S. S.; Yu, Q. L.; Yu, B.; Cai, M. R.; Zhou, F. The synergistic enhancement of microwave absorption performance and corrosion resistance of FeCo by polypyrrole-M16 and TiO_2. *J. Colloid Interface Sci.* **2025**, *686*, 829–843.

[25] Han, Y. X.; Guo, H.; Qiu, H.; Hu, J. W.; He, M. K.; Shi, X. T.; Zhang, Y. L.; Kong, J.; Gu, J. W. Multimechanism decoupling for low-frequency microwave absorption hierarchical Fe-doped Co magnetic microchains. *Adv. Funct. Mater.* **2025**, *35*, 2506803.

[26] Jia, T. M.; Hao, Y. L.; Qi, X. S.; Rao, Y. C.; Wang, L.; Ding, J. F.; Qu, Y. P.; Zhong, W. Interface engineering and impedance matching strategy to develop core@shell urchin-like NiO/Ni@carbon nanotubes nanocomposites for microwave absorption. *J. Mater. Sci. Technol.* **2024**, *176*, 1–12.

[27] Liang, Q. Q.; He, M. K.; Zhan, B. B.; Guo, H.; Qi, X. S.; Qu, Y. P.; Zhang, Y. L.; Zhong, W.; Gu, J. W. Yolk-shell CoNi@N-doped carbon-CoNi@CNTs for enhanced microwave absorption, photothermal, anti-corrosion, and antimicrobial properties. *Nano-Micro Lett.* **2025**, *17*, 167.

[28] Snoek, J. L. Dispersion and absorption in magnetic ferrites at frequencies above one Mc/s. *Physica* **1948**, *14*, 207–217.

[29] Liu, M.; Zhao, B.; Pei, K.; Qian, Y. T.; Yang, C. D.; Liu, Y. H.; Cao, H.; Zhang, J. C.; Che, R. C. An ion-engineering strategy to design hollow FeCo/$CoFe_2O_4$ microspheres for high-performance microwave absorption. *Small* **2023**, *19*, 2300363.

[30] Park, Y.; Park, J. H.; Chul Ro, J.; Suh, S. J. Facile synthesis of FeCo–MnO_2 core–shell nanoparticles as high-frequency microwave absorbers using a two-step method. *Appl. Surf. Sci.* **2023**, *613*, 155976.

[31] Zhong, S. C.; Wang, J. Y.; Zhang, X. T.; Liu, Y.; Wang, X. Y.; Han, X. Z.; Zhang, P. P.; Xia, L. Trilayer core–shell FeCo@SiO_2@lithium-aluminum-silicate microspheres for electromagnetic wave absorption. *ACS Appl. Nano Mater.* **2024**, *7*, 15663–15674.

[32] Gao, K.; Zhao, J. L.; Bai, Z. Y.; Song, W. Z.; Zhang, R. The preparation of FeCo/ZnO composites and enhancement of microwave absorbing property by two-step method. *Materials* **2019**, *12*, 3259.

[33] Huang, W. H.; Song, M.; Wang, S.; Wang, B. K.; Ma, J. C.; Liu, T.; Zhang, Y. N.; Kang, Y. F.; Che, R. C. Dual-step redox engineering of 2D CoNi-alloy embedded B, N-doped carbon layers toward tunable electromagnetic wave absorption and light-weight infrared stealth heat insulation devices. *Adv. Mater.* **2024**, *36*, 2403322.

[34] Cheng, Y. H.; Lan, D.; Jia, Z. R.; Gao, Z. G.; Liu, X. H.; Shi, X. T.; He, M. K.; Guo, H.; Wu, G. L. MOF derivatives anchored to multichannel hollow carbon fibers with gradient structures for corrosion resistance and efficient electromagnetic wave absorption. *J. Mater. Sci. Technol.* **2025**, *216*, 150–164.

[35] Nai, J. W.; Lu, Y.; Yu, L.; Wang, X.; Lou, X. W. Formation of Ni–Fe mixed diselenide nanocages as a superior oxygen evolution electrocatalyst. *Adv. Mater.* **2017**, *29*, 1703870.

[36] Wang, P.; Cheng, L. F.; Zhang, L. T. Lightweight, flexible SiCN ceramic nanowires applied as effective microwave absorbers in high frequency. *Chem. Eng. J.* **2018**, *338*, 248–260.

[37] Wang, G. H.; Ong, S. J. H.; Zhao, Y.; Xu, Z. J.; Ji, G. B. Integrated multifunctional macrostructures for electromagnetic wave absorption and shielding. *J. Mater. Chem. A* **2020**, *8*, 24368–24387.

[38] Liu, J.; Tao, J. Q.; Gao, L. L.; He, X. X.; Wei, B.; Gu, Y. S.; Yao, Z. J.; Zhou, J. T. Morphology-size synergy strategy of SiC@C nanoparticles towards lightweight and efficient microwave absorption. *Chem. Eng. J.* **2022**, *433*, 134484.

[39] Guo, Y.; Guo, X. Y.; Jian, X. High-temperature stability core–shell engineered Ti_3AlC_2@C@SiO_2 for excellent microwave absorbing properties. *Vacuum* **2023**, *212*, 112049.

[40] Huang, M. Q.; Wang, L.; Liu, Q.; You, W. B.; Che, R. C. Interface compatibility engineering of Multi-shell Fe@C@TiO_2@MoS_2 heterojunction expanded microwave absorption bandwidth. *Chem. Eng. J.* **2022**, *429*, 132191.
[41] Shahzad, F.; Alhabeb, M.; Hatter, C. B.; Anasori, B.; Man Hong, S.; Koo, C. M.; Gogotsi, Y. Electromagnetic interference shielding with 2D transition metal carbides (MXenes). *Science* **2016**, *353*, 1137–1140.
[42] Golchinvafa, S.; Masoudpanah, S. M.; Jazirehpour, M. Magnetic and microwave absorption properties of FeCo/$CoFe_2O_4$ composite powders. *J. Alloys Compd.* **2019**, *809*, 151746.
[43] Zhang, B. X.; Wu, C.; Ye, K. C.; Sun, C. Y.; Wang, Z. J. Dual-induced SiC/SME multifunction composite for high-Efficiency broadband electromagnetic wave absorption. *Carbon* **2023**, *213*, 118253.
[44] Liu, J. X.; Hao, H. Q.; Zhang, Y. H.; Wei, L. S.; Cui, Y.; Jing, Q. H.; Yan, S. Q.; Guo, J.; Wang, Z. J. Optimizing the electromagnetic wave absorption bandwidth of SiC/C aerogels using continuous multi-band absorption. *J. Mater. Chem. A* **2025**, *13*, 16061–16069.
[45] Kittel, C. On the theory of ferromagnetic resonance absorption. *Phys. Rev.* **1948**, *73*, 155–161.
[46] Aharoni, A. Exchange resonance modes in a ferromagnetic sphere. *J. Appl. Phys.* **1991**, *69*, 7762–7764.
[47] Dutta, P.; Seehra, M. S.; Thota, S.; Kumar, J. A comparative study of the magnetic properties of bulk and nanocrystalline Co_3O_4. *J. Phys.: Condens. Matter* **2008**, *20*, 015218.
[48] Wang, B. C.; Oomiya, H.; Arakawa, A.; Hasegawa, T.; Sasaki, H.; Ishio, S. Investigation of magnetic anisotropy and magnetic moments of tetragonal distorted $Fe_{1-x}Co_x$ films on $L1_0$ FePt underlayer. *J. Appl. Phys.* **2015**, *117*, 17C709.
[49] Xu, Y. S.; Yao, B. B.; Wang, E. W.; Fan, Y. B.; Lou, B. Z.; Guo, Y. Fabrication of FeCo and $CoFe_2O_4$ nanowire arrays and magnetic properties. *Phys. E: Low-Dimens. Syst. Nanostruct.* **2021**, *130*, 114695.
[50] Xiang, Z.; Song, Y. M.; Pan, D.; Shen, Y. L.; Qian, L. W.; Luo, Z. Y.; Liu, Y. S.; Yang, H. W.; Yan, H.; Lu, W. Coercivity enhancement and magnetization process in $Mn_{55}Bi_{45}$ alloys with refined particle size. *J. Alloys Compd.* **2018**, *744*, 432–437.
[51] Liang, Q.; Hu, X. F.; Li, H. Q.; He, X. X.; Wang, X. R.; Zhang, W. Enhancement of coercivity with reduced grain size in CoCrPt film grown by pulsed laser deposition. *Appl. Surf. Sci.* **2006**, *252*, 4628–4631.
[52] Kneller, E. F.; Luborsky, F. E. Particle size dependence of coercivity and remanence of single-domain particles. *J. Appl. Phys.* **1963**, *34*, 656–658.
[53] Liu, X. G.; Ou, Z. Q.; Geng, D. Y.; Han, Z.; Xie, Z. G.; Zhang, Z. D. Enhanced natural resonance and attenuation properties in superparamagnetic graphite-coated $FeNi_3$ nanocapsules. *J. Phys. D: Appl. Phys.* **2009**, *42*, 155004.

This is an open access article under the terms of the Creative Commons Attribution 4.0 International License (CC BY 4.0, https://creativecommons.org/licenses/by/4.0/).

© The Author(s) 2026. Published by Tsinghua University Press.